Dominant role of OH – and Ti 3+ defects on the electronic structure of TiO 2 thin films for water splitting

Maria-Isabel Mendoza-Diaz, Andrea Balocchi, Kolade Oyekan, Kui Tan, William Vandenberghe, Alain Estève, Carole Rossi

HAL Id: hal-03748775

https://laas.hal.science/hal-03748775

Submitted on 10 Aug 2022

Dominant role of OH⁻ and Ti³⁺ defects on the electronic structure of TiO₂ thin films for water splitting†

Maria Isabel Mendoza Diaz,[a] Andrea Balocchi,[b] Kolade A. Oyekan,[c] Kui Tan,[c] William G. Vandenberghe, [c] Alain Esteve[a] and Carole Rossi*[a]

Anatase/rutile consituted TiO₂ thin films were prepared by sputter-deposition, and the influence of post-annealing step with a narrow window at 200 °C, revealed a gaining factor of 5 in the H₂ production. An in-depth analysis of the photocatalytic performance revealed the dominant role of intermediate states, rather than the hetero-crystalline nature and mesoscale structure. Structural, chemical and optical investigations based on scanning electron microscopy, x-ray diffraction, x-ray photoelectron spectroscopy, UV-visible spectroscopy and photoluminescence supported by ab-initio calculation, correlated the H₂ production with the dual presence of OH⁻ and Ti³⁺ defects in the form of titanium interstitial atoms. In addition, steady-state photoluminescence measurements determined the chemically active role of ethanol, commonly used as a hole scavenger, into inducing deep hole traps upon dissociation on the surface. These results give new directions for the design of TiO₂ based photocatalytic systems for light-driven H₂ production through water splitting, guided by a detailed description of defects present on the electronic structure and their chemical identification.

1. Introduction

The conversion of solar energy into hydrogen (H₂) is an attractive route to allow sustainable and clean energy production.[1,2] Uniquely driven by sunlight, the photocatalysis can dispense with the use of an external electric field source, electrode or electrolyte.[3–6] The most important challenge is to match the transport and lifetime of photo-induced carriers with the chemical processes that drive the water splitting at the photocatalyst surface. Ideally, a semiconductor should absorb over a broad spectral range in order to operate under solar light irradiation. In addition, the conduction (CB) and valence bands (VB) should straddle the water redox potential, i.e. 1.23 eV at pH = 0. In this context, titanium dioxide (TiO₂), despite of its wide band gap (3 - 3.2 eV) and high carrier recombination, still remains a benchmark photocatalyst with high stability, low cost, and low toxicity, all fitting with industrial requirements.[1] The photocatalytic activity of TiO₂ has been reported to depend strongly on both its nanoscale morphology and crystalline structure, where a mixed anatase/rutile structure with a dominant anatase phase has proved to exhibit higher photocatalytic activity than the pristine ones.[6–9] Such properties have been fully investigated for different fabrication techniques such as TiO₂ synthesized powder,[2] sol-gel chemical synthesis,[10] vapor deposited films by sputtering[3] or atomic layer deposition technique.[4] In addition, post-processing treatments such as thermal-annealing,[11] UV-photon irradiations and electrochemical reduction[12] have been reported to modify the crystalline structure, but also, the optical and electronic properties by the creation of localized defects.

It has been found that the presence of either intrinsic defects or extrinsic impurities in nano-TiO₂ materials can induce intrinsic intermediate gap states which are found to play a decisive role determining the charge carrier kinetics.[12] Among these defects, oxygen vacancies (Vo) and Ti interstitials (Ti(i)) are considered the predominant and more common in TiO₂. Photoluminescence (PL) spectroscopy, is a powerful technique for studying the radiative recombination between photogenerated charge carriers, occurring in a few tenths to hundreds of nanometers below the semiconductor surface.[13] Furthermore, PL emission has been reported to elucidate the presence of intermediate states and of the over-all energetic distribution on nanocrystalline TiO₂ materials.[5–9,14–16] Interestingly, Knorr et al.[17] reported two well-defined PL bands in the visible at ~520 nm and ~650 nm for films composed of anatase particles; and, a very defined near IR emission for rutile. These emissions were assigned to distinct transitions of trapped electrons (associated to Vo) and trapped holes, which revealed carrier interphasial electron transport for a mixed anatase/rutile heterostructure. More recently, Mascaretti et al.[16] proposed a slightly different interpretation of the two PL signatures, where the green PL transition was assigned to hole traps induced by oxygen-based radicals; and the red PL transition, was related to electron traps associated to coupled Vo and Ti³⁺ sites. Thus, TiO₂ literature lacks a well-established consensus on the PL processes and about the nature identification of the intermediate states involved in the radiative transitions, which we propose to address in this paper by using Density Functional Theory calculations (DFT). In addition, PL studies have not yet addressed the role of the energetic trap states located in the band gap in relation to the water splitting reaction at the TiO₂ surface/aqueous solution interface. One first limitation comes from the fact that PL properties vary highly with the material elaboration technique. Second, while PL characterization permits to gain insights on the radiative recombination that take place on the nanocrystalline TiO₂, rather than an in-depth analysis of type and concentration of defects present, such as the Vo or Ti³⁺. Third, to the best of

our knowledge, a specific description of the role of defects and in terms of their detailed chemical nature and concentration of oxygen vacancies, Ti interstitials, Ti^{3+} sites, and hydroxyl radicals (OH^-), on H_2 production through water splitting, which represents a crucial step for the design of photocatalytic systems, has never been reported.

The purpose of the present work is to elucidate the mechanisms of water photoreduction by a characterizing the type and nature of defects on TiO_2 thin films and their role on the H_2 production rate from the viewpoint of the electronic structure. We consider nanostructured anatase/rutile TiO_2 thin films prepared by sputter-deposition, exhibiting different activities in direct water splitting experiments based on different types and quantity of defects induced by thermal treatments. The paper discusses these performances in relation to basic TiO_2 properties, including structural, morphological, optical, and chemical properties leading to a rationale of their impact on photocatalysis. An in-depth understanding on their defect states is addressed by performing PL experiments and DFT calculations considering: i) the effect of post-deposition thermal treatments in reducing atmosphere; and ii) the selective scavenging of photogenerated charges to localize the gap states and chemical nature of the most pertinent defects that correlate with water splitting photo-activity.

2. Experimental

2.1 TiO₂ films deposition. Physical vapor deposition (PVD) of TiO_2 was conducted by direct current magnetron sputtering of a Titanium target (99.999% purity) on silicon and quartz substrates. Before loading, substrates were cleaned by O_2 plasma. Pressure of the chamber was 8×10^{-8} Pa. A gas mixture of 40% O_2 and 60% Ar (99.9999% purity each) was set with a pressure of 1.07 Pa. DC power of reactive plasma was 1200 W. The deposition cycles were adjusted to obtain a film with a thickness of 270 nm chosen in coherence with previously reported study (3). Annealing treatments were conducted for three samples at 200, 550 and 700 °C in an inert atmosphere (N_2 99.9999% purity flow 2 l min^{-1}). The heating ramp of 5 °C min^{-1} and the annealing time 1 h.

2.2 Experimental characterization. The morphological and structural analyses were performed by scanning electron microscopy (SEM, S-4800, Hitachi), high resolution transmission electron microscopy (HRTEM , JEOL 2100F) with detector STEM HAADF (JEOL) and EDS SDD detector (Ultim-Max) in TEM, HRTEM and diffraction modes; atomic force microscopy (AFM, Dimension ICON, Bruker) and grazing incidence X-ray diffractometry (GI-XRD, Bruker D8 Discover system). Residual stress was measured by mechanical profilometry (KLA Tencor, P17). Photocatalytic experiments were carried by gas chromatography (GC, Perkin-Elmer Clarus 580) to measure the H_2 production rate. Samples were placed into a quartz reactor (60 mL) filled with an aqueous solution (10 mL, DI water and 35% v/ v ethanol Technic, 99.9% purity, CAS: 64-17-5) under Ar atmosphere. Sample were irradiated by a Xenon light lamp (Cermax® PE300B-10F) with a spectral region of 300 to 1100 nm. The hydrogen evolution rate was normalized with respect to the light flux received by the sample,

corrected for the UV absorption and calculated after 24 h of irradiation. Optical properties were studied by UV–Vis spectroscopy (PerkinElmer Lambda 650 UV–Vis spectrometer), for which samples were deposited on quartz; and by X-ray photoelectron spectroscopy (XPS, PerkinElmer, PHI System) performed at room temperature with an Al Kα (1486.6 eV) X-ray source at a residual gas pressure < 3.99×10^{-7} Pa chamber pressure, and using a 16-channel detector with a hemispherical analyzer. Electron Microprobe analysis (EMP, Cameca SXFive FE microprobe) was operated at low voltage (7 kV) for a sub-µm X-ray generation volume, measurements were obtained by setting the probe depth in a range of 228.1 to 256 nm from the surface to the bulk of the film. Atomic composition of the films was obtained using a quantitative analysis by comparing the intensities of the characteristic X-rays for elemental O and Ti with the respective intensities of standard natural minerals. Photoluminescence spectra were recorded at room temperature on a custom-made set-up. The excitation was provided by a frequency-doubled picosecond Titanium:Saphire laser (Spectra Physics, Tsunami) at λ = 355 nm (1 mW average power, 1 ps pulse duration and 80 MHz repetition frequency). The luminescence spectrum was dispersed by a 500 mm focal length imaging spectrometer (Princeton Instrument, Acton 2500i) and its intensity recorded with a silicon UV-enhanced, liquid-nitrogen-cooled charge-coupled device detector (Princeton Instrument, Pylon Excelon 400). Measurements in ethanol and vacuum, were performed in a quartz cuvette and in a in a cryostat connected to a diaphragm pump, respectively.

2.3 Computational details. Spin-polarized DFT calculations were performed using the generalized gradient approximation (GGA) with the Perdew-Burke-Ernzehof (PBE)(18) exchange-correlation functional as implemented in the Vienna ab-initio Simulation Package (VASP).(19–22) Projector augmented waves (PAW) pseudopotentials were employed to describe ion-electron interactions,(23,24) and the electron wave functions were expanded in terms of plane wave basis sets, with a kinetic energy cutoff of 400 eV. Wavefunctions were optimized until the change in total energy was less than 10^{-6} eV. We employed Grimme's DFT-D3 method to include dispersion contributions to the energy values.(25) The anatase (101) supercell, with lattice parameters a = b = 3.8073 Å and c = 9.7318 Å(26,27) was built using a vacuum of 10 Å between anatase slabs along the direction normal to the surface (**Supplementary Information Figure S6-1**). The 1 × 3 supercell surface contains a total of 108 atoms, and the bottom layer of TiO_2 was held fixed while all other atoms were allowed to relax in all directions during minimization of the total energy. The Brillouin zone was sampled at the gamma point. The density of states calculations where performed using the DFT+U method. Several model surfaces

have been generated to include a series of defects and adsorbed species as detailed in the **Supplementary Information S6**.

3. Results and discussion

3.1 Structural and morphological characterization

TiO₂ films were deposited on silicon substrates and annealed at 200, 550 and 700 °C, hereafter named T-AD (as-deposited), T-200, T-550 and T-700, respectively. The effect of the annealing temperature was analyzed by GI-XRD to investigate the changes of phase structure. **Figure 1a** displays the XRD patterns of the films. T-AD sample shows the characteristic peaks of PVD polycrystalline TiO₂ at 2ϑ = 25.37, 37.89, 38.72, 48.22, 53.88, 53.30, 62.77 and 70.42° corresponding to the anatase planes (101), (004), (112), (200), (105), (211), (204) and (215); (3,28) and at 2ϑ = 27.42, 54.37 and 68.93°, corresponding to the rutile planes (110), (211) and (301),(29,30) respectively. Both structures were confirmed with COD database, patterns number 1010942 and 9009083, for anatase and rutile, respectively. No peaks related to impurities are observed. Upon annealing at 200 °C (T-200), the intensities of the peaks corresponding to the anatase planes (101), (004), (112), (105) and (211), increase with respect to the as-deposited film (T-AD); and a further increase is observed by annealing at 550 °C (T-550). However, by annealing at 700 °C (T-700), the intensities of the anatase peaks become weaker, while the peaks associated to rutile planes (110), (211) and (301), increase notably. Subsequently, new rutile peaks also appeared at 2ϑ = 36.10 and 44.17°, associated to (101) and (210) planes, respectively. The major change is observed in the intense narrow peaks located at 2ϑ = 25.37 and 27.42° that correspond to tetragonal anatase plane (101) and rutile plane (110). For T-AD, the ratio of the intensity anatase (101) peak with respect to rutile (110) is 3.5; and it increases up to 3.7 and 4.2 by annealing at 200 (T-200) and 550 °C (T-550), respectively. Upon annealing at 700 °C (T-700), this ratio decreases drastically to 0.3. In order to quantify the composition of each crystalline phase, the percentage composition of rutile was estimated using Equation 1:

$$[R]\ \% = 1/(1 + 0.884\ {^{I_A}/_{I_R}}) \times 100 \qquad (1)$$

Where I_A and I_R correspond to the area of the anatase (101) and rutile (110) peaks, respectively. The number 0.884 is a scattering coefficient. Therefore, the anatase composition is equal to [A] = 100 − [R].(31) Results reported in **Table 1** show that anatase phase dominates the film structure for the T-AD with 60.58% and, it increases almost linearly by annealing at 200 °C and furthermore to 71.36% at 550 °C. Inversely, by increasing the thermal treatment up to 700 °C, the anatase phase transforms greatly into rutile: 71.36% of rutile.

The crystallite diameter of anatase and rutile was also estimated by using the Scherrer's formula (**Supplementary Information S1**).(32) As reported in **Table 1**, the crystallite diameter of anatase does not change notably upon annealing, with 21.00, 17.11, 25.52 and 21.96 nm for T-AD, T-200, T-550 and T-700, respectively. In contrast, rutile crystallite exhibits minor changes by annealing at 200 °C, with relatively small crystallite diameters (6.95 and 5.53 nm, for T-AD and T-200).
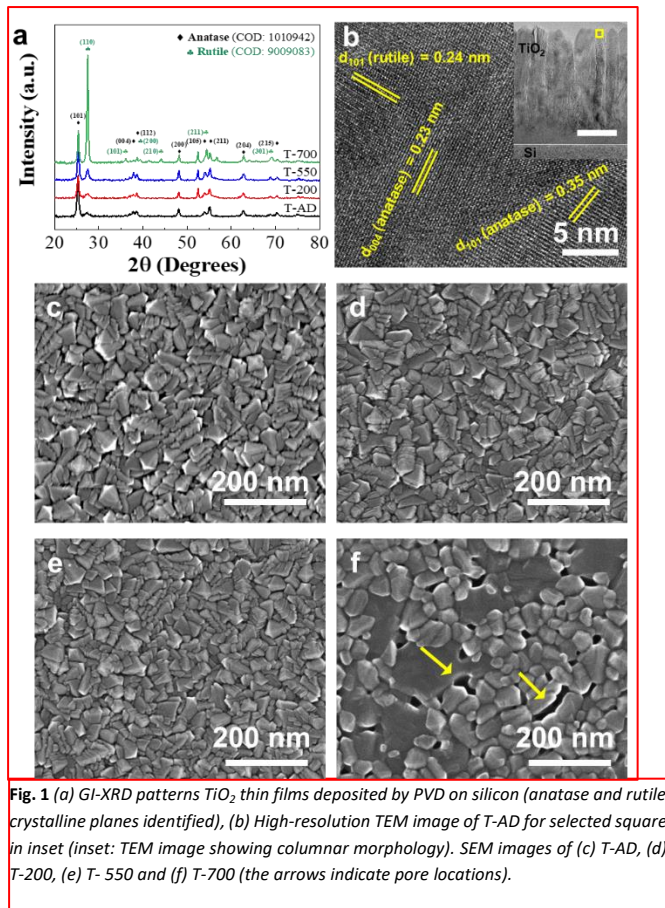
Fig. 1 *(a) GI-XRD patterns TiO₂ thin films deposited by PVD on silicon (anatase and rutile crystalline planes identified), (b) High-resolution TEM image of T-AD for selected square in inset (inset: TEM image showing columnar morphology). SEM images of (c) T-AD, (d) T-200, (e) T- 550 and (f) T-700 (the arrows indicate pore locations).*

Moreover, a noticeable increase is observed at higher temperatures (13.55 and 24.66 nm, for T-550 and T-700). These results demonstrate that both crystalline structures are present in the polycrystalline films where anatase is the predominant phase even when films are annealed to 200 and 550 °C.

The morphology of the cross-section was observed by TEM, Figure 1b-inset shows an HAADF-STEM image of the cross-section of T-AD exhibiting the characteristic columnar growth of TiO₂ deposited by PVD. Next, high-resolution images were obtained from the grains, the HRTEM image (Figure 1b) displays a d-spacing of 0.35 and 0.23 nm that agree well with the reported spacing for the (101) and (004) lattice planes of anatase; and a d-spacing of 0.24 nm, ascribed to the (101) lattice planes of rutile.(15,33) Also Moiré fringes where found repeatedly (**Supplementary Information S1 Figure S1-1**), which have been reported for the combination of lattice fringes of anatase and rutile.(34) The selected area electron diffraction (SAED) image (**Supplementary Information Figure S1-1)** corroborated the polycrystalline structure of the film as well as the d-spacing identified for anatase and rutile by HRTEM.

Surface morphology was observed by SEM. In agreement with XRD and TEM results, the polycrystalline surface is composed of grains (see **Figure 1c-f**) with well-defined boundaries and faceted shape of the columnar morphology for TiO₂ deposited by PVD.(3) Average grain size and average pore size are reported in **Table 1** as AGS and APS (details in **Supplementary Information Figure S2-3**). Upon annealing at 550 °C the morphology remains almost unchanged, indicating a

Table 1. Crystalline structure and dimensions of crystallite, grains, and pores of TiO2 thin films deposited on silicon.

Sample	Crystalline structure (wt%)	Err.	Crystallite diameter [1] (nm)	AGS [2] (nm)	APS [3] (nm)	Average Stress [4] (MPa)	Std. Dev.
T-AD	60.58 (A), 39.42 (R)	5.12 10⁻⁵	21.00 ± 0.14 (A), 6.95 ± 0.05 (R)	32.0 ± 0.9	8.8 ± 0.5	191.0	7.46 10⁻⁸
T-200	66.36 (A), 33.64 (R)	5.12 10⁻⁵	17.11 ± 0.11 (A), 5.53 ± 0.04 (R)	30.4 ± 0.8	6.3 ± 0.3	315.5	7.78 10⁻⁸
T-550	71.36 (A), 28.64 (R)	5.12 10⁻⁵	25.52 ± 0.17 (A), 13.55 ± 0.09 (R)	29.2 ± 0.7	6.6 ± 0.4	605.5	8.24 10⁻⁸
T-700	21.63 (A), 78.37 (R)	5.02 10⁻⁵	21.96 ± 0.15 (A), 24.66 ± 0.16 (R)	59.1 ± 2.0	15.6 ± 0.7	638.3	7.76 10⁻⁸

A and R denote anatase and rutile, respectively.

[1] Calculated with Scherrer formula from XRD patterns.

[2] Average grain size measured by SEM.

[3] Average pore size measured by SEM.

[4] Average stress measured by profilometry.

negligible effect of the temperature on the film morphology; yet, the grains and pores size decreases slightly, from ~32 to 29 nm and ~8 to 6 nm, for AGS and APS, respectively; leading to a more compact structure. However, by annealing at 700 °C, AGS increases notably to 59 nm. Likewise, APS doubles. Note that some big grains in T-700 show the remaining embossed grain boundaries of the individual merged grains. Surface roughness was calculated by AFM mapping over 1 μm^2 area. The calculated roughness is 4.21, 4.21, 4.29 and 5.44 nm for T-AD, T-200, T-550 and T-700 samples, respectively. 2D and 3D images are shown in **Supplementary Information Figure S1-4**.

These observations confirm the XRD analysis, where up to 550 °C, anatase structure dominates the composition and its respective crystallite diameter does not change significantly, except a slight densification of the film, whereas at 700 °C, a rich rutile phase is obtained with a marked bigger crystallite and pore sizes. The structural changes affect the homogeneity of the film and can be correlated with internal stresses accumulated during the film growth. The average tensile stress values are shown in **Table 1** and **Table S2** (calculation details in **Supplementary Information S1**). The residual stress increases with temperature. Yet, even if the dominant phase changes to rutile upon annealing at 700 °C, the residual stress caused by annealing from 550 to 700 °C is small, whereas a drastic change is observed by annealing from 200 to 550 °C (315.50 to 605.50 MPa). This increase of the tensile stress can be ascribed to the change in the film microstructure.(35)

3.2 Photocatalytic activity

H_2 production through photocatalysis represents a sustainable solution since it can be obtained through solar energy and biomass derivatives, such as methanol, ethanol, and sugars; these are considerate renewable products as they can be produced from biomass resources *i.e.*, energy plants, industrial wastewaters, as well as plastic waste.(36,37) Among these derivates, ethanol is readily produced from alcoholic

fermentation of cellulose, and starch(38) and is known as a model hole scavenger as it has been reported to enhance the hydrogen evolution reaction of TiO2.(15,39) Hence this study uses a water-ethanol solution is used for the gas chromatography characterization, the H_2 production rates for each TiO_2 sample is presented in **Figure 2**. As supplement, temporal H_2 evolution is provided in **Supplementary Information Figure S2**. Except for the sample annealed at 200 °C, with 2.0 $\mu mol\ W^{-1}\ h^{-1}$, all other films production rate is below 0.4 $\mu mol\ W^{-1}\ h^{-1}$. T-200 exhibits a 4.6 enhancement factor compared to the reference sample T-AD. This suggests a very narrow annealing pathway in order to optimize the TiO_2 water splitting performance. Note that at this stage, the linear increase of anatase structure with the temperature up to 550 °C does not coincide with the H_2 production enhancement. Importantly, this indicates that the nanoscale surface morphology and structural composition are not the determinant factors in maximizing the TiO_2 water splitting process, pointing to the potential role of the TiO2 surface/subsurface chemical states. In the next sections, an in-depth study of the effect of the thermal annealing on the TiO2
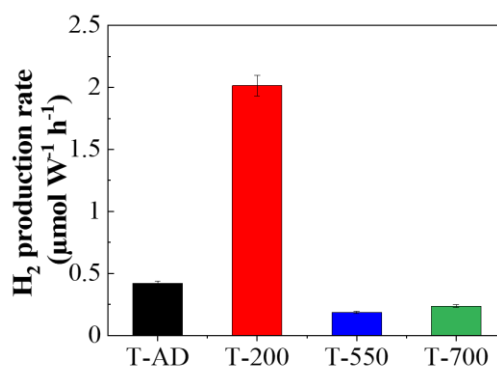
Fig. 2 *Normalized H_2 production rate of TiO_2 thin films under UV+vis irradiation.*

Table 2. *Details of EMP measurements and XPS Ti 2p and O 1s spectra of TiO$_2$ thin films.*

Samples	O / Ti bulk atomic ratio [1]	Ti^{3+} / Ti^{4+} ratio	O1s HE / LE [2] ratio	O / Ti surface atomic ratio [3]	VBE (eV) [4]
T-AD	2.07 ± 4.8 10^{-3}	3.04 10^{-2} ± 2.1 10^{-6}	0.96 ± 1.1 10^{-4}	1.92 ± 2.0 10^{-3}	2.85 ± 5.0 10^{-3}
T-200	2.08 ± 3.5 10^{-3}	4.64 10^{-2} ± 4.0 10^{-4}	1.14 ± 1.1 10^{-4}	1.91 ± 2.6 10^{-3}	2.69 ± 5.0 10^{-3}
T-550	2.02 ± 3.4 10^{-3}	2.77 10^{-2} ± 2.5 10^{-4}	0.59 ± 2.9 10^{-5}	1.80 ± 2.2 10^{-3}	2.89 ± 5.0 10^{-3}
T-700	2.02 ± 3.2 10^{-3}	4.16 10^{-2} ± 3.9 10^{-4}	0.62 ± 3.0 10^{-5}	1.77 ± 2.3 10^{-3}	2.58 ± 5.0 10^{-3}

[1] Calculated with electron microprobe analysis (EMP).

[2] High energy (HE) and low energy components (LE) of O 1s XPS spectra.

[3] Calculated with XPS spectroscopy.

[4] Relative to Fermi level.

films will be conducted by chemical, optical and theoretical studies to shed light on its relationship with the photocatalytic activity results. In order to establish a hierarchy of the potential contributions, the TiO$_2$ stoichiometry (surface and bulk), defect presence, their electronic structure and chemical nature identification is analyzed next.

3.3 Chemical characterization

Table 2 reports bulk and surface chemical nature and oxidation states upon annealing. While a TiO$_{2.0}$ bulk stoichiometry is expected, at least for the as-deposited sample, PVD deposition led to slightly higher oxygen atomic ratio in all samples. Yet, T-AD and T-200 have the highest oxygen content with TiO$_{2.07}$ and TiO$_{2.08}$ stoichiometry, respectively. Consistently, by annealing above 550 °C the process reduces slightly the films, resulting in a stoichiometry stabilizing at 2.02 for both T-550 and T-700.

Figure 3a-d shows the deconvoluted Ti 2p core-level XPS spectra. The two distinct peaks corresponding to Ti 2p$_{3/2}$ and 2p$_{1/2}$ are present in all the samples (see binding energies in **Supplementary Information Table S3)**. Both peaks are dominated by the Ti^{4+} oxidation state component, located at 459.16 and 464.90 eV in T-AD; with a minor presence of the reduced Ti^{3+} species component, located at 457.72 and 463.32 eV in T-AD. Upon annealing, a slight shift to lower energies of both Ti 2p$_{2/3}$ and 2p$_{1/2}$ peaks is observed. This has been associated to the presence of Ov defects.(40) To analyze the Ti^{4+} and Ti^{3+} components, gaussian deconvolution was carried out. From the Ti^{3+}/Ti^{4+} ratios reported in **Table 2**, it is clear that T-200 presents the maximum number of Ti^{3+} species (4.6 10^{-2} ratio), followed by T-700 (4.2 10^{-2} ratio).

The presence of Ti^{3+} sites is commonly associated with the formation of Vo,(41,42) resulting in surface excess charge in the form of localized Ti^{3+} sites with an unpaired electron.(43) Jin *et al.*(44) showed that annealing in inert atmospheres can induce the removal of oxygen atoms creating a lone pair of electrons neighboring two Ti^{4+} sites, which are then oxidized to Ti^{3+}. This was also documented by Sajines *et al.*(45) who states that by removing an oxygen atom, two adjacent titanium atoms become fivefold coordinated. Therefore, the Ov is negatively charged in order to maintain the local charge neutrality. This charge is shared by the two adjacent titanium atoms changing its oxidation state from Ti^{4+} to Ti^{3+}. Note that Ti^{3+} species can also be attributed to Ti(i), as Finazzi *et. al.*(46) demonstrated
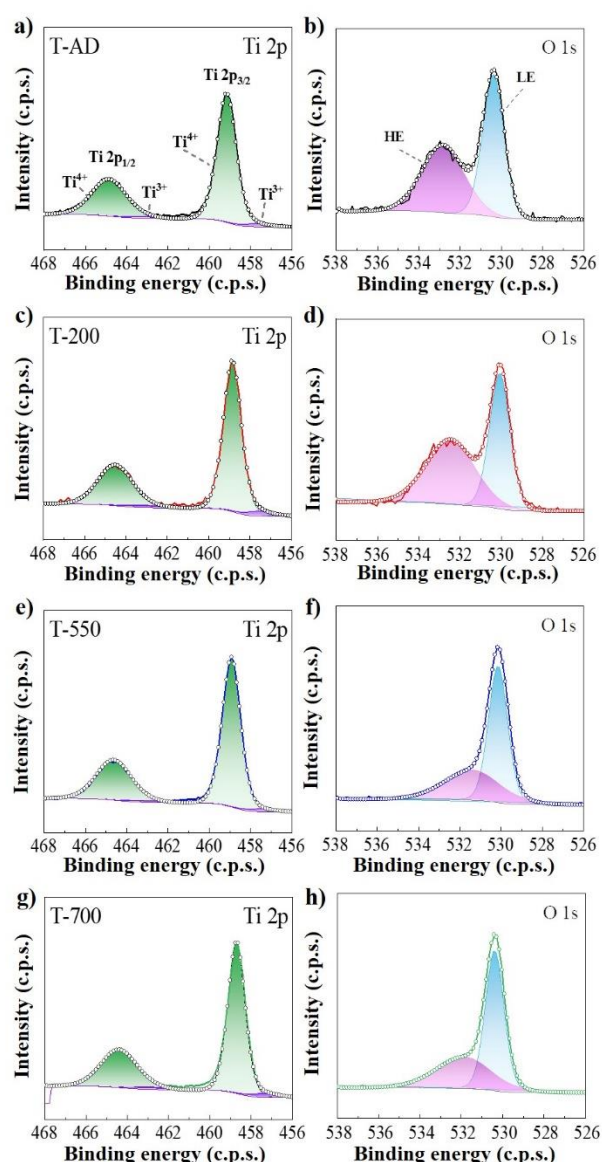
Fig. 3 *Ti 2p and O 1s XPS core level spectra of TiO$_2$ thin films (a, b) T-AD, (c,d) T-200, (e, f) T-550 and (g,h) T-700.*

when a Ti(i) is located in a host crystal, it spontaneously transforms into a Ti^{3+} ion with a single electron localized, surrounded by a polaronic distortion which favors its

localization; whereas the remaining electrons of Ti^{3+} are distributed on the titanium ions of the lattice with a small exchange interaction. However, XPS characterization does not allow to clearly differentiate the origin of Ti^{3+} species (*i.e.,* due to Vo or Ti(i) formation). However, the increased intensity of Ti^{3+} species in T-200 and T-700 samples, denotes a higher density of defects which contrast with the structural characterization and photocatalytic activity, where both samples show remarkably dissimilar characteristics.

The O 1s core-level XPS deconvoluted spectra (**Figure 3**) exhibit two defined components in all samples, the first at high energy (noted HE), commonly assigned to weakly adsorbed oxygen species in the form of hydroxyl groups (−OH) or bounded to carbon (−C) (as contaminants) and/or lattice oxygen atoms bounded to undercoordinated titanium atoms, making it an indirect signature of Vo.(40) And, the second component at lower energy (noted LE) is ascribed to the metal oxide bond, in this case the O^{-2} bound to Ti^{+4}. In T-AD these components are located at 532.8 and 530.3 eV, respectively.

A shift of the HE component (OH⁻, O−C) to lower binding energies is seen for T-550 and T-700, decreasing from ~532.6 to ~531.6 eV; whereas the LE component (O−Ti) remains at ~530 eV for all the samples. Components associated with −OH groups may also be influenced by defects created by thermal treatment.(45) Within the HE component, the OH⁻ species position has been located at 532.2 eV.(10,47) Note that surface bound OH⁻ radicals have been found to generate hole traps,(42) which will be discussed later in the paper. The HE / LE ratio (**Table 2**) points out a higher content of OH⁻ radicals for low temperatures samples, notably T-200, followed by T-AD, which decreases upon annealing above 550 °C. This suggests that the presence of such species in T-200 is related to intermediate states within the band gap possibly improving the charge transfer.

Regarding the surface stoichiometry, the O/Ti atomic ratio reported in **Table 2**, was calculated from the XPS core level spectra (calculation details in **Supplementary Information S3**). Contrary to the atomic ratio of the bulk obtained by EMP, all the samples exhibit a lower oxygen content on the surface, even below the expected $TiO_{2.0}$ stoichiometry. Interestingly, T-AD presents the most stoichiometric surface with $TiO_{1.92}$, which decreases consistently upon increasing the annealing temperature until $TiO_{1.77}$ for T-700.

In summary, thermal annealing above 550 °C affects notably the surface stoichiometry, exhibiting a highly reduced surface, whereas the bulk stoichiometry remains closest to $TiO_{2.0}$. This can be related to H_2 production results, where samples T-200 and T-AD exhibit the best performances. T-AD and T-200 samples present a similar stoichiometry: the surface composition is the closest to $TiO_{2.0}$, whereas the bulk presents a richer oxygen content, (higher atomic content compared to T-550 and T-700). Yet, T-200 sample which exhibits the best H_2 production yield, possess a higher density of defects associated to Ti^{3+} and OH⁻ species, both pointing to the dominant role of surface defects. In order to investigate further on these defects in relation to the photocatalytic activity, optical

characterization (UV-vis and PL) and first principles calculations are discussed in the next sections.

3.4 Optical properties and electronic structure

Transmittance spectra was used to calculate the optical band gap (E_{op}) and Urbach energy (E_u) of the different samples (**Supplementary Information S4**). The values plotted in **Figure 4**, range from 3.28 to 3.38 eV and 165.07 to 205.80 meV, for E_{op} and E_u, respectively**.** The indirect band gap values for TiO_2 reported in literature for anatase and rutile are 3.2 and 3.0 eV.(48) This could explain the higher E_{op} calculated for T-200 and T-550, since they have a higher content of anatase; consequently, T-700 has a lower E_{op} since the dominant phase is rutile. The Urbach energy is closely related to the structural disorder in the band gap since it is determined by the width of the band gap tails, which are formed due to the presence of defect states in the band gap.(49) Note that the T-200 optical band gap is wider than that of T-AD by +0.03 eV. Also, the structure disorder is relatively high in T-200 (E_u = 189.24 meV), which suggests the presence of intermediate states in the band gap. Upon annealing at 550 °C the Urbach energy is the lowest, but the optical band gap is the widest. These results contribute to elucidate the difference between these two samples, since both samples have a similar structure in terms of anatase to rutile ratio, and a similar morphology; yet the photocatalytic activity drops dramatically for T-550. This is also in coherence with XPS analysis, indicating that upon annealing at 200 °C, more defective sites are induced, that contribute somehow to the water splitting reaction.

The valence band edge (VBE) can be obtained from the low energy range of the XPS spectrum (spectra in **Supplementary Information Figure S4-3**), this allows to precisely locate the conduction band edge (CBE). By using the VBE and the calculated E_{op} and the fermi level (E_F = 0), CBE was calculated to be at 0.49, 0.68, 0.49 and 0.77 eV above the E_F for T-AD, T-200, T-550 and T-700, respectively. These values are in coherence with the reported n-type nature of TiO_2.(16)

In order to locate the intermediate states in the band gap, PL measurements were carried out. **Figure 5** shows the spectra recorded in vacuum. Two clear signals are present in samples T-
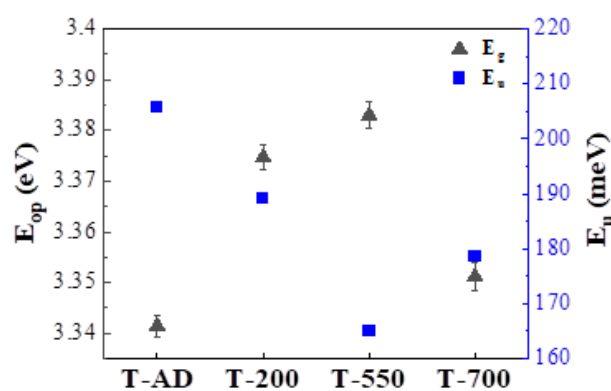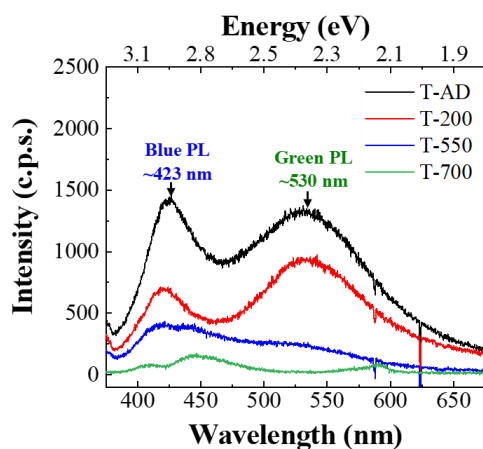

Fig. 4 *Variation of the optical band gap and Urbach energy of TiO_2 films deposited on quartz. Data obtained from transmittance spectra. E_u error bars range from 0.04 to 0.06 meV.*

AD, T-200 and T-550, located at ~425 and ~530 nm, which hereafter will be named blue and green PL, respectively. Upon increasing the annealing temperature above 550 °C, the intensities decrease. At 700 °C the blue and green PL signals are completely quenched, and a minor band appears at 450 nm. The quenching is ascribed to the rich rutile composition of T-700, whose characteristic PL signals are in the near-IR region.(17)

The blue PL is well defined in T-AD and T-200 compared to T-550 which features broader bands. Even though these samples and T-550 have a rich anatase composition, they exhibit a very different PL spectrum. Therefore, the blue and green PL signals cannot be mainly assigned to the anatase rich structure. Interestingly, the relative intensity of the blue to green PL bands is higher for T-AD and T-550, while for T-200 is the opposite. PL responses have been reported in a similar range, from 400 to 800 nm, but with one single broad component for anatase films annealed above 500 °C composed of particles(8) or deposited by pulsed laser deposition.(16) A PL feature similar to green PL centered at ~550 nm, was also obtained for sol-gel nanostructured anatase with a small portion of brookite; and it was assigned to Vo, which are ascribed to displacements of the oxygen atoms position in the bond lengths (Ti–O) creating a degree of structural disorder.(10) Furthermore, for anatase films, two defined PL bands have been reported: a green component at ~520 nm, assigned to recombination between electrons in the CB and deeply-trapped holes; and a red component at ~650 nm, assigned to the recombination between holes in VB and deeply-trapped electrons. Yet for a mixed anatase/rutile phase, the second radiative transition was quenched.(26)

Moreover, the band to band transitions are not present in the PL spectra, since the signals are located at lower energy than the calculated E_{op} (< 3.34 eV in T-AD). Hence, the PL bands can be assigned to intermediate states located in the band gap. Based on the most recent studies,(8,16) the blue PL signal is attributed to the recombination of electrons in the CB with hole traps located in the band gap, whereas, the green PL signal is attributed to the recombination of deep trapped electrons with holes in the VB, which will be demonstrated later by steady-
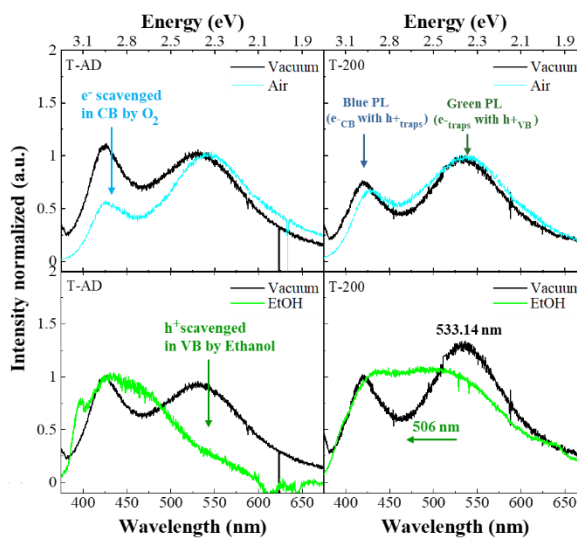
state PL measurements by exposing the samples to scavenging agents. Importantly, a direct correlation can be presumed between the enhanced photocatalytic activity, *i.e.* the H_2 production of samples T-AD and T-200, and the presence of intermediate states associated with Ti^{3+} and OH^- species. Indeed, studies reported that the introduction of Ti^{3+} species accompanied by high Vo concentration leads to the formation of defect states with energies of 0.75 to 1.18 eV below the CB; hence, since these energies are closer to the CB, these defects states act as electron traps.(50) On the other hand, OH^- radicals are related to the presence trapped holes as mentioned previously.(42)

The next study will focus on T-AD and T-200 samples, which shown notable intensities of the PL bands and a high concentration of defects, notably Ti^{3+} and OH^- species. Yet, it is necessary to corroborate the assignation of the radiative recombination to specific electron or holes traps. This will be addressed in the following section by steady-state PL measurements conducted in different scavenging media (air and ethanol) in order to elucidate the quenching of specific transitions. Based on the later, the next two sections are focus on T-AD and T-200 samples, which shown notable intensities of the PL bands and a high concentration of defects according to XPS. In Section 3.5, the PL radiative recombination will be assigned to specific electron and hole traps. This will be addressed by PL measurements conducted with scavenging agents of holes and electrons separately. Next, in the final section, the traps will be correlated to the surface and subsurface defects and the stoichiometry findings.

3.5 Identification of intermediate states by PL with scavenging agents

Air and ethanol were used in steady-state PL measurements to elucidate the quenching of specific transitions. While oxygen present in air can scavenge electrons from the CB, ethanol is known to be an efficient hole scavenger. Therefore, if the

Fig. 5 *Photoluminescence spectra excited at 355 nm in vacuum of TiO₂ thin films. Blue and green PL bands signals assigned to the recombination of electrons in the CB with hole traps, and to deep trapped electrons with holes in the VB.*

Fig. 6 *Photoluminescence spectra excited at 355 nm of TiO₂ thin films T-AD and T-200 in different media. Blue lines: air, green: ethanol; and black: vacuum. Upper plots: normalized to green PL band, bottom: normalized to blue PL band.*

intermediate states exist, the photogenerated charges (electrons or holes) will be trapped at these localized states and will not take part to the radiative recombination. Upon air exposure (**Figure 6** blue plots), the blue PL intensity in T-AD sample is quenched from 1 to 0.5 a.u., meaning that oxygen scavenges the electrons on the CB, thus quenching the signal associated to recombination of CB electrons with hole traps. In contrast, the blue PL intensity of T-200 in air decreases just from 0.75 to 0.70 a.u, and it shifts to slightly higher wavelengths, meaning that a recombination within the band gap with a lower energy remains active under air. This could be attributed to the presence of shallow electron traps below the band gap where electrons are trapped after excitation before recombining with the hole traps. Next, the green PL remains at the same wavelength upon air exposure in both samples, this is consistent with the presence of deep electron traps that prevent the electrons from being scavenged by oxygen, and subsequently undergo recombination with holes in the VB.

Experiments have identified the presence of deep electron traps for intermediate states located around $0.75 - 1.00$ eV below the CBE.(16) Therefore, by using the calculated E_{og}, the green PL for T-200 with an energy of ~2.32 eV (530 nm), which accounts for the recombination of trapped electrons with holes in the VB, indicates that the electron traps are located at 1.0 eV below the CB, hence evidencing its role as deep electron traps. In addition, the blue PL (~2.92 eV) which accounts for recombination of trapped holes with electrons, determines the position of the electron at traps located at -0.44 eV below the CB for T-200 (-0.39 for T-AD). This corroborates the shallow electron traps in both samples, such traps have been correlated to titanium ions in the lattice, which are characterized by a small interaction within the lattice, compared to Ti^{3+}; therefore do not affect greatly the total stability.(46) As explained in Section 3.3, the titanium ions in the lattice are originated by the donated electrons of the reduced Ti^{3+} species induced by Ti(i). In order to avoid misinterpretation of the bands associated to the radiative recombination at the TiO_2/ethanol interface, PL spectra of ethanol was recorded in order to identify its characteristic PL response (**Supplementary Information Figure S5).** The spectra of the films in ethanol (**Figure 6** green plots) are normalized with respect to the blue PL, as it is the most stable band and not affected by scavenging. As expected, the green PL of T-AD sample is quenched, since ethanol scavenges the holes in the VB, eliminating the possibility of radiative recombination with trapped electrons. In T-200, the green PL is mildly quenched by comparison with vacuum, this indicates that the holes in the VB are partially scavenged. This could be explained by the presence of holes in deep traps which cannot be scavenged by ethanol.

The green PL signal shifts to higher energies (+0.12 eV), positioning the radiative emission at ~506 nm (Cyan PL). After considering the recombination of holes positioned at these traps with electrons located in shallow traps below the CB, the Cyan PL is associated to deep hole traps. It has been reported that deep holes traps are chemically equivalent to surface-bound OH^- radicals which have been proposed as an important intermediate in the oxidation reaction of the water splitting

process by various authors.(42) This agrees with the XPS results where the T-200 exhibits the highest HE/LE O 1s ratio, plus the position of the HE component is assigned to OH^- radicals. To shed more light in the identification of the defects that are associated with the observed radiative recombination, DFT calculations are performed on model surfaces screening the defects under consideration in the present paper.

3.6 Chemical defects correlation to intermediate states by DFT

Density of states (DOS) of a stoichiometric 1 x 3 anatase (101) slab (pristine slab) with specific defective model surfaces were performed to elucidate the creation of intermediate states. The scheme of the slab anatase structures are shown in **Supplementary Information S6**. The DOS shows the CB and VB well defined on the right and left extremes, respectively, on the energy axis. **Figure S6-1** (see **Supplementary Information S6**) shows the DOS of the pristine slab, where no intermediate states are observed in the band gap. As mentioned in the previous sections, Ti^{3+} species are correlated of Ti^{3+} sites coupled to Vo (Ti^{3+}–Vo), but also to the presence of Ti(i). **Figure 7a** shows the DOS of the slab with a subsurface Ti(i), leading to the formation of shallow states, and deep states, close to the CB, therefore deep and shallow electron traps; this in coherence with the nature of Ti^{3+} species originated from the localization of Ti(i).

In addition, the DOS of the slab with an Ov localized on Ti^{3+} atoms (**Supplementary Information Figure S6-3**) also shows the presence of deep electron traps, corroborating the presence of Ti^{3+} sites neighboring Ov in addition to the creation of shallow electron states, are expected, since Ti(i) provide more electrons to the lattice than the Vo.(46) Next, in the presence of adsorbed −OH groups on Ti^{3+} sites in **Figure 7b**, shallow hole traps are created close to the VBE, which confirms the assignment of the blue PL to shallow hole traps.(26) By combining both defects Ti(i)-slab with an adsorbed OH^- (**Figure 7c**), shallow and deep
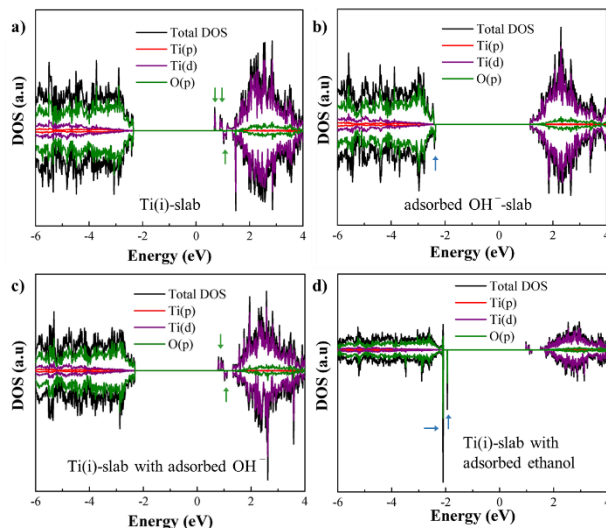

Fig. 7 *DOS plots of stoichiometric 1 x 3 anatase (101) slab with (a) a Ti interstitial Ti(i), (b) an adsorbed OH^-, (c) Ti(i)-slab with an adsorbed OH^- and (d) Ti(i)-slab with an adsorbed ethanol molecule. The arrows indicate intermediate states, green: electron traps, blue: hole traps.*

electron traps remain present, and interestingly, the deep traps are more prominent; yet, the hole traps do not appear. In order to emulate the hole scavenging as in steady-state PL, **Figure 7d** shows the T(i)-slab after dissociative chemisorption of ethanol onto TiO_2. Here, the appearance of hole traps is evident, meaning that in a defective structure with Ti(i), the traps near the VB relocate creating deep hole traps. The DOS results indicate a clear correlation between the creation of intermediate states and the presence of Ti(i), Vo localized on Ti^{3+} atoms, and OH^- adsorbates located on the surface and subsurface.

According to the XPS results, T-200 sample, followed by T-AD showed a higher concentration of such species, in the form of Ti^{3+} and OH^-, compared to the T-550 and T-700. The presence of shallow and deep electron traps is therefore associated to Ti(i) which transform to Ti^{3+} sites coupled to Vo (Ti^{3+}–Vo), both present in T-AD and T-200.

Hence, the increased Ti^{3+}/Ti^{4+} ratio for T-200 compared with T-AD, can now be attributed to a higher concentration of Ti(i). Furthermore, since the O1s HE component was already ascribed to OH^- species due to their shifted position (Section 3.3), both samples also possess a high content of adsorbed OH^-, where T-200 also exhibited an increased O1s HE/LE ratio, accounting for the presence of deep hole traps. In addition, OH^- bond species have been proposed as an important intermediate in photocatalytic oxidation processes,(42) promoting the charge transport. Both contributions (*i.e.,* Ti^{3+} and OH^-) lead to an extended region of electron deep traps in T-200. This is confirmed by the remarked quenching of the blue PL on air for T-AD (**Figure 6**), whereas in T-200, electrons are trapped in deep states avoiding scavenging by oxygen. Finally, the presence of deep hole traps is elucidated by the adsorption of ethanol on a slab with Ti(i) in the subsurface. Since T-200 possess a higher concentration of Ti(i), upon ethanol exposure, the holes located in shallow states are trapped in these deep traps and avoid scavenging by ethanol, this explains the broadening of the blue PL into the lower-wavelength (cyan PL) and the quenching of the green PL for T-AD, where such deep traps are not present. **Figure 8** summarizes the main findings of this study just discussed, based on a mapping of states and radiative processes within the gap for T-AD and T-200.
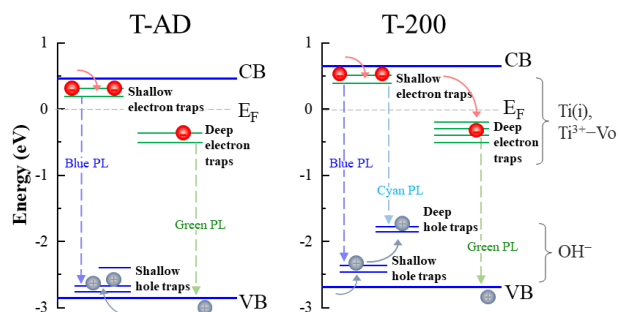
Fig. 8 *Band gap scheme with localized intermediate traps of electron and holes in TiO_2 thin films T-AD and T-200. PL radiative recombination are represented by dashed lines. Electron traps are created by the presence of Ti^{3+} species associated to Ti interstitials Ti(i) and oxygen vacancy Vo located on Ti^{3+} sites, whereas hole traps are associated to OH^- radicals adsorbed on the surface.*

4. Conclusions

Structural and morphological studies, chemical and optical-electronic spectroscopy techniques supported by photoluminescence measurements and DFT calculations were used for the determination of the band structure and its correlation to the photocatalytic activity of TiO_2 films prepared by sputtering and annealed at different temperatures from 200 °C to 700 °C in neutral atmosphere. We observe a narrow post annealed temperature window, 200 °C, that enhances H_2 production (×5 compared to other samples). The structural properties and SEM observations point to a similar rich anatase phase for the films annealed up to 550 °C, pushing the structural aspects to a secondary role for what concerns H_2 production. Rather, we find that the higher photocatalytic TiO_2 performance correlate with the dual presence of OH^- and Ti^{3+}. While Ti^{3+} was commonly associated to oxygen vacancies in the literature, we demonstrate that interstitial Ti atoms is also a potential contributor to be associated with the Ti^{3+} PL signature. Moreover, we highlight the chemically active role of ethanol, commonly used as a hole scavenger, inducing deep hole traps upon dissociation on the surface. We believe that the paper gives new directions to optimize the TiO_2 for achieving the water splitting mechanisms, and more generally to extend its photocatalytic activity.

Author Contributions

Maria Isabel Mendoza Diaz: Conceptualization, Methodology, Investigation, Validation, Formal analysis, Writing – original draft, Writing – review & editing, Visualization. Alain Esteve: Formal analysis, Supervision. Writing – review & editing. Carole Rossi: Funding acquisition, Formal analysis, Supervision. Writing – review & editing. Andrea Balocchi : PL experiments and analysis. Review & editing. Kolade A. Oyekan: DFT calculations. William G. Vandenberghe: supervision of DFT calculations. Kui Tan: XPS experiments and analysis.

Conflicts of interest

There are no conflicts of interest to declare.

Acknowledgements

Abbreviations

CB, conduction band; VB, valence band; CBE, conduction band edge; VBE, valence band edge; PL, photoluminescence, Vo, oxygen vacancies; Ti(i), titanium interstitials, OH^-, hydroxyl species.

References

1. Kumaravel V, Mathew S, Bartlett J, Pillai SC. Photocatalytic hydrogen production using metal doped TiO2: A review of recent advances. Appl Catal B Environ. 2019 May;244:1021–64.

2. Sanchez-Martinez A, Koop-Santa C, Ceballos-Sanchez O, López-Mena ER, González MA, Rangel-Cobián V, et al. Study of the preparation of TiO $_2$ powder by different synthesis methods. Mater Res Express. 2019 May 24;6(8):085085.

3. Mendoza-Diaz MI, Cure J, Rouhani MD, Tan K, Patnaik SG, Pech D, et al. On the UV–Visible Light Synergetic Mechanisms in Au/TiO $_2$ Hybrid Model Nanostructures Achieving Photoreduction of Water. J Phys Chem C. 2020 Nov 19;124(46):25421–30.

4. Nasr M, Abou Chaaya A, Abboud N, Bechelany M, Viter R, Eid C, et al. Photoluminescence: A very sensitive tool to detect the presence of anatase in rutile phase electrospun TiO $_2$ nanofibers. Superlattices Microstruct. 2015 Jan;77:18–24.

5. Mercado CC, Knorr FJ, McHale JL, Usmani SM, Ichimura AS, Saraf LV. Location of Hole and Electron Traps on Nanocrystalline Anatase TiO $_2$. J Phys Chem C. 2012 May 17;116(19):10796–804.

6. Rex RE, Yang Y, Knorr FJ, Zhang JZ, Li Y, McHale JL. Spectroelectrochemical Photoluminescence of Trap States in H-Treated Rutile TiO $_2$ Nanowires: Implications for Photooxidation of Water. J Phys Chem C. 2016 Feb 18;120(6):3530–41.

7. Dozzi MV, D'Andrea C, Ohtani B, Valentini G, Selli E. Fluorine-Doped TiO $_2$ Materials: Photocatalytic Activity vs Time-Resolved Photoluminescence. J Phys Chem C. 2013 Dec 5;117(48):25586–95.

8. Pallotti DK, Passoni L, Maddalena P, Di Fonzo F, Lettieri S. Photoluminescence Mechanisms in Anatase and Rutile TiO $_2$. J Phys Chem C. 2017 Apr 27;121(16):9011–21.

9. Rex RE, Knorr FJ, McHale JL. Surface Traps of TiO $_2$ Nanosheets and Nanoparticles as Illuminated by Spectroelectrochemical Photoluminescence. J Phys Chem C. 2014 Jul 31;118(30):16831–41.

10. Silva Junior E, La Porta FA, Liu MS, Andrés J, Varela JA, Longo E. A relationship between structural and electronic order–disorder effects and optical properties in crystalline TiO $_2$ nanomaterials. Dalton Trans. 2015;44(7):3159–75.

11. Shi J, Chen J, Feng Z, Chen T, Lian Y, Wang X, et al. Photoluminescence Characteristics of TiO $_2$ and Their Relationship to the Photoassisted Reaction of Water/Methanol Mixture. J Phys Chem C. 2007 Jan 1;111(2):693–9.

12. Liu B, Zhao X, Yu J, Parkin IP, Fujishima A, Nakata K. Intrinsic intermediate gap states of TiO2 materials and their roles in charge carrier kinetics. J Photochem Photobiol C Photochem Rev. 2019 Jun;39:1–57.

13. Erbe A, Nayak S, Chen YH, Niu F, Pander M, Tecklenburg S, et al. How to Probe Structure, Kinetics, and Dynamics at Complex Interfaces In Situ and Operando by Optical Spectroscopy. In: Encyclopedia of Interfacial Chemistry [Internet]. Elsevier; 2018 [cited 2022 Feb 23]. p. 199–219. Available from: https://linkinghub.elsevier.com/retrieve/pii/B978012409547 2140612

14. Leytner S, Hupp JT. Evaluation of the energetics of electron trap states at the nanocrystalline titanium dioxide/aqueous solution interface via time-resolved photoacoustic spectroscopy. Chem Phys Lett. 2000 Nov;330(3–4):231–6.

15. Zhang WF, Zhang MS, Yin Z, Chen Q. Photoluminescence in anatase titanium dioxide nanocrystals. Appl Phys B Lasers Opt. 2000 Feb 1;70(2):261–5.

16. Mascaretti L, Russo V, Zoppellaro G, Lucotti A, Casari CS, Kment Š, et al. Excitation Wavelength- and Medium-Dependent Photoluminescence of Reduced Nanostructured TiO $_2$ Films. J Phys Chem C. 2019 May 2;123(17):11292–303.

17. Knorr FJ, Mercado CC, McHale JL. Trap-State Distributions and Carrier Transport in Pure and Mixed-Phase TiO $_2$: Influence of Contacting Solvent and Interphasial Electron Transfer. J Phys Chem C. 2008 Aug 1;112(33):12786–94.

18. Perdew JP, Burke K, Ernzerhof M. Generalized Gradient Approximation Made Simple. Phys Rev Lett. 1996 Oct 28;77(18):3865–8.

19. Kresse G, Furthmüller J. Efficient iterative schemes for *ab initio* total-energy calculations using a plane-wave basis set. Phys Rev B. 1996 Oct 15;54(16):11169–86.

20. Kresse G, Furthmüller J. Efficiency of ab-initio total energy calculations for metals and semiconductors using a plane-wave basis set. Comput Mater Sci. 1996 Jul;6(1):15–50.

21. Kresse G, Hafner J. *Ab initio* molecular dynamics for liquid metals. Phys Rev B. 1993 Jan 1;47(1):558–61.

22. Kresse G, Hafner J. *Ab initio* molecular-dynamics simulation of the liquid-metal–amorphous-semiconductor transition in germanium. Phys Rev B. 1994 May 15;49(20):14251–69.

23. Kresse G, Joubert D. From ultrasoft pseudopotentials to the projector augmented-wave method. Phys Rev B. 1999 Jan 15;59(3):1758–75.

24. Blöchl PE. Projector augmented-wave method. Phys Rev B. 1994 Dec 15;50(24):17953–79.

25. Berne BJ, Ciccotti G, Coker DF. Classical And Quantum Dynamics In Condensed Phase Simulations: Proceedings Of

The International School Of Physics. In: World Scientific. 1998. p. 385–404.

26. Liu X, Fu J. Electronic and elastic properties of the tetragonal anatase TiO2 structure from first principle calculation. Optik. 2020 Mar;206:164342.

27. Burdett JK, Hughbanks T, Miller GJ, Richardson JW, Smith JV. Structural-electronic relationships in inorganic solids: powder neutron diffraction studies of the rutile and anatase polymorphs of titanium dioxide at 15 and 295 K. J Am Chem Soc. 1987 Jun;109(12):3639–46.

28. Cure J, Cocq K, Nicollet A, Tan K, Hungria T, Assie-Souleille S, et al. A Beehive Inspired Hydrogen Photocatalytic Device Integrating a Carbo-Benzene Triptych Material for Efficient Solar Photo-Reduction of Seawater. Adv Sustain Syst. 2020 Sep;4(9):2000121.

29. Secundino-Sánchez O, Diaz-Reyes J, Sánchez-Ramírez JF, Jiménez-Pérez AJL. Structural and optical characterization of the crystalline phase transformation of electrospinning TiO2 nanofibres by high-temperatures annealing. Rev Mex Física. 2019 Sep 2;65(5 Sept-Oct):459–67.

30. Li D, Dai S, Goullet A, Carette M, Granier A, Landesman JP. Annealing and biasing effects on the structural and optical properties of PECVD-grown TiO2 films from TTIP/O2 plasma. J Mater Sci Mater Electron. 2018 Aug;29(15):13254–64.

31. Fu X, Clark LA, Yang Q, Anderson MA. Enhanced Photocatalytic Performance of Titania-Based Binary Metal Oxides: TiO$_2$/SiO$_2$ and TiO$_2$/ZrO$_2$. Environ Sci Technol. 1996 Jan 1;30(2):647–53.

32. Yue GH, Yan PX, Wang J. Study on the preparation and properties of copper nitride thin films. J Cryst Growth. 2005 Feb;274(3–4):464–8.

33. Miao L, Jin P, Kaneko K, Terai A, Nabatova-Gabain N, Tanemura S. Preparation and characterization of polycrystalline anatase and rutile TiO2 thin films by rf magnetron sputtering. Appl Surf Sci. 2003 May;212–213:255–63.

34. Lee GH, Zuo JM. TEM observation of growth and phase transformation in nanometer-sized titanium oxide powder. J Mater Sci. 2011 Mar;46(6):1780–8.

35. Matěj Z, Kužel R, Nichtová L. X-Ray Diffraction Analysis of Residual Stress in Thin Polycrystalline Anatase Films and Elastic Anisotropy of Anatase. Metall Mater Trans A. 2011 Nov;42(11):3323–32.

36. Puskelova J, Baia L, Vulpoi A, Baia M, Antoniadou M, Dracopoulos V, et al. Photocatalytic hydrogen production using TiO2–Pt aerogels. Chem Eng J. 2014 Apr;242:96–101.

37. Uekert T, Kuehnel MF, Wakerley DW, Reisner E. Plastic waste as a feedstock for solar-driven H$_2$ generation. Energy Environ Sci. 2018;11(10):2853–7.

38. Gautam R, Nayak JK, Daverey A, Ghosh UK. Emerging sustainable opportunities for waste to bioenergy: an overview. In: Waste-to-Energy Approaches Towards Zero Waste [Internet]. Elsevier; 2022 [cited 2022 Jul 21]. p. 1–55. Available from: https://linkinghub.elsevier.com/retrieve/pii/B9780323853873 00001X

39. Nada A, Barakat M, Hamed H, Mohamed N, Veziroglu T. Studies on the photocatalytic hydrogen production using suspended modified photocatalysts. Int J Hydrog Energy. 2005 Jul;30(7):687–91.

40. Kruse N, Chenakin S. XPS characterization of Au/TiO2 catalysts: Binding energy assessment and irradiation effects. Appl Catal Gen. 2011 Jan;391(1–2):367–76.

41. Liang L, Ling P, Li Y, Li L, Liu J, Luo Q, et al. Atmospheric CO2 capture and photofixation to near-unity CO by Ti3+-Vo-Ti3+ sites confined in TiO2 ultrathin layers. Sci China Chem. 2021 Jun;64(6):953–8.

42. Bahnemann DW, Hilgendorff M, Memming R. Charge Carrier Dynamics at TiO$_2$ Particles: Reactivity of Free and Trapped Holes. J Phys Chem B. 1997 May 1;101(21):4265–75.

43. Glezakou VA, Rousseau R. Shedding light on black titania. Nat Mater. 2018 Oct;17(10):856–7.

44. Jin C, Liu B, Lei Z, Sun J. Structure and photoluminescence of the TiO2 films grown by atomic layer deposition using tetrakis-dimethylamino titanium and ozone. Nanoscale Res Lett. 2015 Dec;10(1):95.

45. Sanjinés R, Tang H, Berger H, Gozzo F, Margaritondo G, Lévy F. Electronic structure of anatase TiO$_2$ oxide. J Appl Phys. 1994 Mar 15;75(6):2945–51.

46. Finazzi E, Di Valentin C, Pacchioni G. Nature of Ti Interstitials in Reduced Bulk Anatase and Rutile TiO$_2$. J Phys Chem C. 2009 Mar 5;113(9):3382–5.

47. Cottre T, Fingerle M, Kranz M, Mayer T, Kaiser B, Jaegermann W. Interaction of Water with Atomic Layer Deposited Titanium Dioxide on p-Si Photocathode: Modeling of Photoelectrochemical Interfaces in Ultrahigh Vacuum with Cryo-Photoelectron Spectroscopy. Adv Mater Interfaces. 2021 Jun;8(11):2002257.

48. Lin H, Li L, Zhao M, Huang X, Chen X, Li G, et al. Synthesis of High-Quality Brookite TiO$_2$ Single-Crystalline Nanosheets with Specific Facets Exposed: Tuning Catalysts from Inert to Highly Reactive. J Am Chem Soc. 2012 May 23;134(20):8328–31.

49. Choudhury B, Dey M, Choudhury A. Defect generation, d-d transition, and band gap reduction in Cu-doped TiO2 nanoparticles. Int Nano Lett. 2013 Dec;3(1):25.

50. Xing M, Zhang J, Chen F, Tian B. An economic method to prepare vacuum activated photocatalysts with high photo-

activities and photosensitivities. Chem Commun. 2011;47(17):4947.